THE JOURNAL OF PHYSICAL CHEMISTRY C

Article

Cite This: J. Phys. Chem. C 2019, 123, 14999−15008

pubs.acs.org/JPCC

Tunable Electronic and Optical Properties of a Planar Hydrogenated AsSi Hybrid Nanosheet: A Potential Wide Water-Splitting Photocatalyst

W.X. Zhang,[†] H. Wang,[†] C.H. Shi,[†] S.Y. Liu,[†] S.Y. Chang,[†] and C. He*[,‡]

[†]School of Materials Science and Engineering, Chang'an University, Xi'an 710064, China

[‡]State Key Laboratory for Mechanical Behavior of Materials, School of Materials Science and Engineering, Xi'an Jiaotong University, Xi'an 710049, China

Supporting Information

ABSTRACT: Two-dimensional (2D) layered structures have recently drawn worldwide attention in material science and device physics because of their intriguing electrical and optical properties. In this paper, the structural, electronic, and magnetic properties of fully and partially hydrogenated AsSi nanosheets (NSs) are investigated by first-principles calculations based on density functional theory. Moreover, the potential as photocatalysts for water splitting is also studied. The results demonstrate that hydrogenated H atoms have a great influence on the electronic properties of the AsSi NS. By decorating their surface, fully and semihydrogenated AsSi NSs still exhibit ferromagnetism states and are predicated to be metallic or semiconductive depending on the surface coverage. Calculation results show that a more stable configuration of the semihydrogenated AsSi NS (AsSiH) is the one wherein all H atoms are adsorbed onto Si atoms, which is a semiconductor as the applied biaxial strains are from −6 to 9% and the band gap reaches its maximum with 4% tensile strain. More remarkably, AsSiH NSs with tensile strains up to 9% exhibit proper band gaps, valence, and conduction band positions of the reduction and oxidation levels in visible-light-driven water splitting. The diverse electronic and optical properties highlight hydrogenated AsSi NSs' potential applications in efficient electronic and optoelectronic devices.

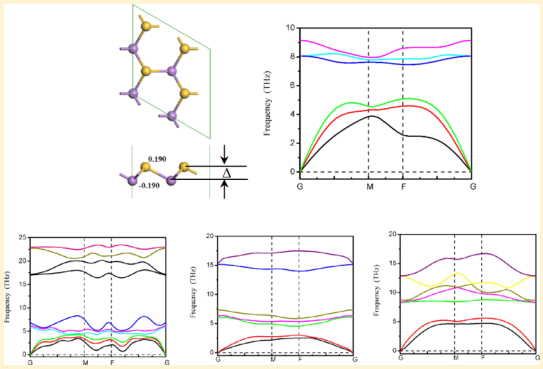

1. INTRODUCTION

This decade, stimulated by the preparation of graphene, two-dimensional (2D) crystals have attracted more attention because of their extraordinary properties and potential applications in the field of nanoelectronics.[1−4] To expand the application of 2D materials, many scientists are beginning to explore more similar materials, including BN,[5,6] GaN,[7,8] germanane,[9] MoS_2,[10] antimonene,[11] and black phosphorus with a puckered honeycomb structure.[12,13] Theoretical predictions and experimental results show that these 2D layered materials have a variety of electronic properties, including metallic, semiconducting, superconducting, and even a very high mobility of topological insulators,[13] which is different from or even better than their volume counterparts. With many promising applications in nanoelectronics and optoelectronics applications,[14,15] both the fundamental scientific importance and the promise of practical applications make the exploration of new layered materials with novel properties a vigorous field of research in condensed matter physics and materials research.

At present, the 2D materials synthesized mainly have the group IV elements, such as graphene,[1] silicene,[16] germanium,[17] and SnX_2 films,[18] and group V elements, such as arsenic, antimony, and bismuth.[19,20] The energetically favorable configuration of silicene has been confirmed to be a buckled structure, which has been recently predicted theoretically and synthesized experimentally.[21−26] Especially, Zhao et al. have reported that because of the related low-buckled geometry with partial sp^3 hybridization, the intrinsic properties of silicene differ from that of graphene with pure sp^2 hybridization in some aspects, for example, a larger SOC gap of 1.55 meV, and a tunable band gap, an easier valley polarization, and much smaller thermal conductivity of 3−65 W/mK.[27] Among the heavier group V elements, monolayer antimonene has been successfully prepared by micromechanical exfoliation, oxidation−reduction,[28] and CVD techniques.[29−31] The monolayer covers a band gap and has superior carrier mobility and thus is promising candidates for nanoelectronics and optoelectronics.

Water-splitting photocatalysis is an effective method to solve the energy shortage at this stage. Considering the response characteristics of their light, with recognition, is extremely an important application of 2D semiconductor with different band

Received: February 19, 2019
Revised: May 5, 2019
Published: May 23, 2019

DOI: 10.1021/acs.jpcc.9b01630
J. Phys. Chem. C 2019, 123, 14999−15008

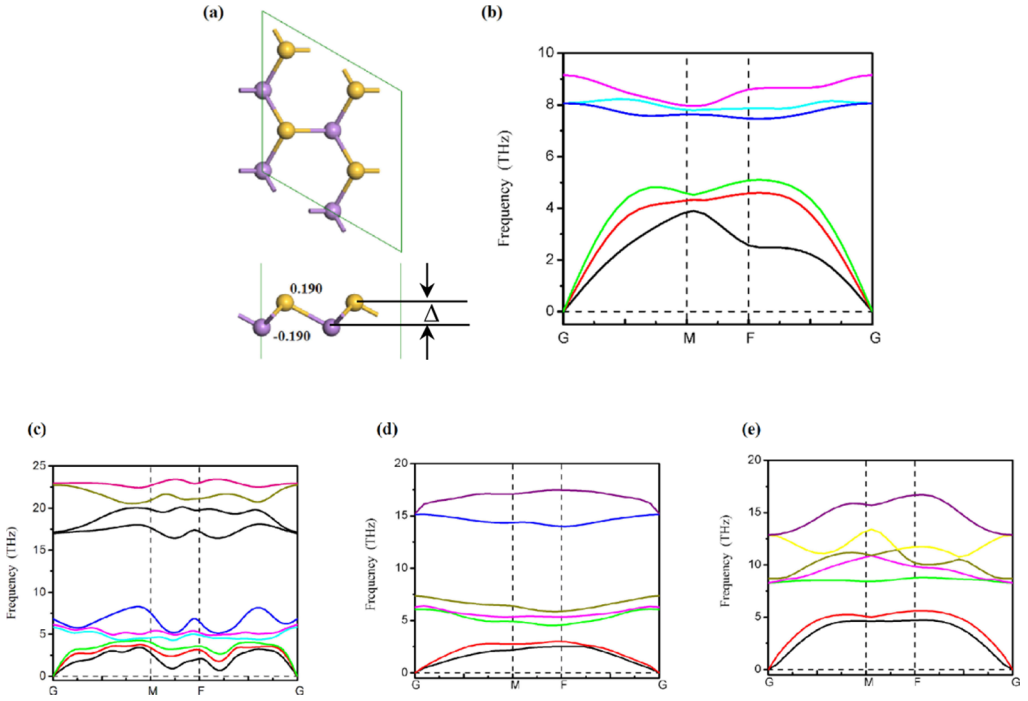

Figure 1. Optimized geometric structure (a) and the calculated phonon dispersion curves (b) of the AsSi nanosheet. The pink and yellow balls denote As and Si atoms, respectively. Phonon-dispersion curves of three hydrogenated AsSi NS systems: (c) HAsSiH NS; (d) HAsSi NS; and (e) AsSiH NS.

gap energies in optoelectronic devices. Photocatalytic water-splitting reaction to produce hydrogen is an important key to solve the problem of energy crisis and environment pollution.[32−35] However, the development of 2D semiconductor optoelectronic devices is limited to the band gap of the most existing 2D materials.[36] More interestingly, a low-dimensional semiconductor material exhibiting metallic behavior for electron spins with one orientation and insulating behavior for the spins with the opposite orientation is highly desirable in spintronic nanodevices.[4,37] Because 2D nanosheets (NSs) have a higher surface-to-volume ratio compared to bulk materials, chemical functionalization plays an important role in determining their properties, paving a way to tune the band gaps and magnetic properties of the semiconductor NSs.[4] Hydrogenation and halogenation are known to serve as local doping sites that significantly change the properties of 2D nanomaterials and are reported to have potential applications in spintronic devices.[38−43]

Correspondingly, many efforts were devoted to the functionalization of silicone[44,45] and arsenene,[46,47] and lots of interesting results have been reported. Half-hydrogenated silicene without substrates turns out to be a ferromagnetic semiconductor,[44] whereas fully hydrogenated silicene generates about 2 eV indirect band gap.[45] Zhang et al. have reported the electronic properties of arsenene and fully hydrogenated arsenene.[47] Very recently, Scheer et al. have successfully synthesized the pnictogen−silicon analogue of benzene, $[(PhC(NtBu)_2)_3Si_3As_3]$ molecules.[48] The enhanced stability and quasi-planar geometric properties of Si_3As_3 provide a new direction for our future research and inspire us to use it as a building block to design 2D planar materials combined with silicon and arsenic atoms. The above research provides an interesting opportunity for realizing tunable electronic and photoelectric properties of NSs by controlling different surface modification and strain engineering.

Yet, a systematically theoretical understanding of electronic, photocatalytic, and magnetic properties of the hydrogenated functionalized 2D hybrid arsenene and silicene hybrid nanosheet (AsSi NS), from mixing As and Si atoms in an alternating arrangement in a chair conformer, remains unclear. These studies have a great significance for the application of arsenic and silicon atoms in the field of electronic and optoelectronic devices.

Therefore, the structural characteristics and the possibilities of tuning electronic properties of surface-hydrogenated AsSi NSs are extensively carried out by first-principles calculations based on density functional theory calculations with vdW corrections (DFT-D). We verified their stabilities by calculating binding energies and phonon dispersions. Under equilibrium conditions, the electronic properties of the AsSi NS can be tuned by decorating H atoms. After decorating, fully and semihydrogenated AsSi NSs still exhibit ferromagnetism states and are predicated to be metallic or semiconducting depending on the percentage of surface coverage. A more stable configuration of semihydrogenated AsSi NS (AsSiH) is the one wherein all H atoms are adsorbed onto Si atoms with a band gap of 2.040 eV (2.327 eV from hybrid functional calculations). More remarkably, a tensile strain-engineered AsSiH monolayer exhibits proper band gap, and the band edges straddling water redox potentials in the visible-light-driven water splitting reaction. These studies provide us guidance to future experiments and a deep understanding of the novel properties, which has a potential application foreground in the fields of nanoelectronics, water splitting, and so on.

2. COMPUTATIONAL METHODS

The simulations in this paper were based on DFT, which was supported by a CASTEP package with a norm-conserving pseudo-potential.[49] The generalized gradient approximation

DOI: 10.1021/acs.jpcc.9b01630
J. Phys. Chem. C 2019, 123, 14999−15008

Table 1. Calculated Structural Parameters of the Fully and Partially Hydrogenated AsSi Nanosheet[a]

structure	a	E_b	d_{H-As}	d_{As-Si}	d_{Si-H}	Δ	θ	E_g
AsSi	3.60			2.356		0.556	99.588	half-metallic
HAsSiH	4.32	−3.248	1.529	2.498	1.500	0.169	118.532	metallic
HAsSi	3.97	−2.090	1.561	2.454		0.475	108.261	0.544 (0.596)
AsSiH	3.66	−3.317		2.355	1.501	0.860	102.039	2.040 (2.327)

[a]The lattice constants a (in Å), buckling parameter Δ (in Å), d_{H-As}, d_{Si-As}, and d_{Si-H} are the bond lengths of H−As, As−Si, and Si−H, respectively (in Å). The bond angle (θ) in (deg), binding energy (E_b) in (eV per supercell), and band gap E_g in (eV) obtained by using the PBE (outside the parentheses) and HSE06 hybrid (in the parentheses) functionals are given for semiconductors structures.

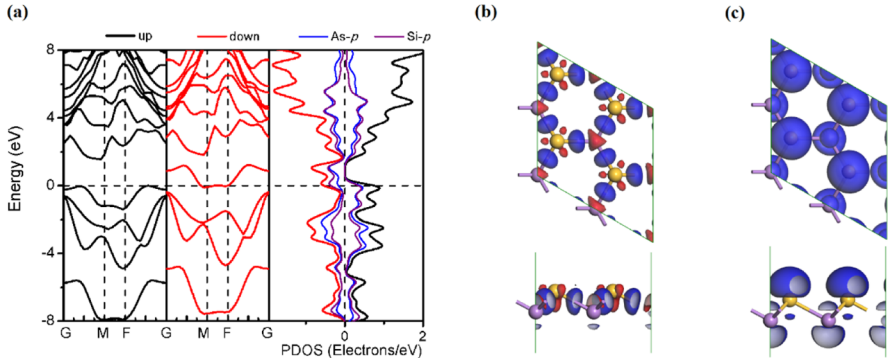

Figure 2. Band structure, total DOS, and PDOS of AsSi nanosheet (a). Black and red solid lines denote spin up and spin down band, respectively. The Fermi level is set to zero and indicated by black dashed line. PDOS results are also shown for selected orbitals. Blue and red denote positive and negative wave function contours in charge density difference (b), respectively, and the isosurface values are ±0.05 e/Å^3. The blue surface corresponds to the isosurfaces of spin density distribution ($\Delta\rho = \rho_{up} - \rho_{down}$) (c) with the isosurfaces of 0.03 e/Å^3.

(GGA) and Perdew−Burke−Ernzerhof (PBE)[50] were adopted for the exchange-correlation potential to optimize structures. Norm-conserving pseudo-potential[51] was chosen for both spin-polarized and spin-unpolarized computations. The Brillouin zone was sampled by 6 × 6 × 1 (10 × 10 × 1) k-points,[52] and the energy cutoff of 650 eV was chosen in the calculations. Increasing the k-points mesh to 8 × 8 × 1 for all structures in the geometry optimization did not increase the convergence of the total energy. These setups were proven to be accurate enough for describing the results after careful test calculations. The nearest distance between NSs in neighboring cells was greater than 20 Å to ensure no interactions between different layers.[8] For geometry optimization, both the cell and atomic positions were allowed to fully relax to find the equilibrium states until the convergence tolerances of energy, maximum force, and displacement of 1 × 10^{-5} eV, 0.03 eV/Å, and 0.001 Å were reached, respectively.[8] Because the GGA−PBE exchange correlation functional tended to underestimate the band gap of semiconductors, the HSE06 in CASTEP was also used to check the electronic band structure of semiconductors.

Binding energy (E_b) could be used to prove the stability of the hydrogenated AsSi systems. The formula for E_b is[10,46]

$$E_b = \frac{1}{n}(E_{total} - E_{AsSi} - nE_H) \quad (1)$$

where E_{total}, E_{AsSi}, and E_H are the energy of hydrogenated AsSi systems, AsSi NS with the same supercell, and an isolated hydrogen atom, respectively. n is the number of primitive cell.

The CASTEP code was used to perform the ab initio molecular dynamics (MD) simulations in order to study the thermal stability of fully and partially hydrogenated AsSi NSs in the canonical (NVT) ensemble. Volume V and temperature T are constants, and N is the atom number. T is imposed by the Nose algorithm. The simulation temperature was set at 300 K. The total simulation time was set to be 2.0 ps with a time step of 1.0 fs. The GGA−PBE functional was adopted.[53−55]

The electronic distributions of AsSi NSs were carried out by Mulliken charge analysis, which was performed using a projection of a linear combination of atomic orbital basis and to specify quantities such as atomic charge, bond population, charge transfer, and so forth.[51] The obtained relative values of the charge e, but not the absolute magnitude, display a high degree of sensitivity to the atomic basis set and a relative distribution of charge.[7,56]

3. RESULTS AND DISCUSSION

The stable low-buckled geometry of minimum energy with relaxed lattice constant of the monolayer AsSi NS is a = 3.60 Å through structural optimization. A 2 × 2 × 1 supercell of monolayer AsSi NS containing 8 atoms is constructed. From the structural relaxing calculations, the total-energy optimization of the AsSi NS yields a layered buckled honeycomb-like structure with threefold—coordinated As and Si atoms in the hexagonal unit cell in Figure 1a, similar to the cases of arsenene and silicene, whose original stable configurations are also buckled hexagonal.

Table 1 lists the calculated bond lengths, buckling parameters, and electronic properties for the AsSi NS. The bond length of d_{As-Si} is 2.356 Å, which is intermediate between the Si−Si bond length in silicene of 2.252 Å[57] and As−As bond length in arsenene of 2.51 Å,[58] and is in agreement with the previous theoretical result of silicene-like SiAs.[59] Compared with graphene, the larger As−Si interatomic distance weakens the $\pi-\pi$ overlaps, which leads to wrinkle in the c direction of the AsSi NS. This results in a low-buckled structure with sp^3-like hybrid orbitals. The buckling height (Δ) along the z direction is defined as 0.556 Å after the structural relaxation.

DOI: 10.1021/acs.jpcc.9b01630
J. Phys. Chem. C 2019, 123, 14999−15008

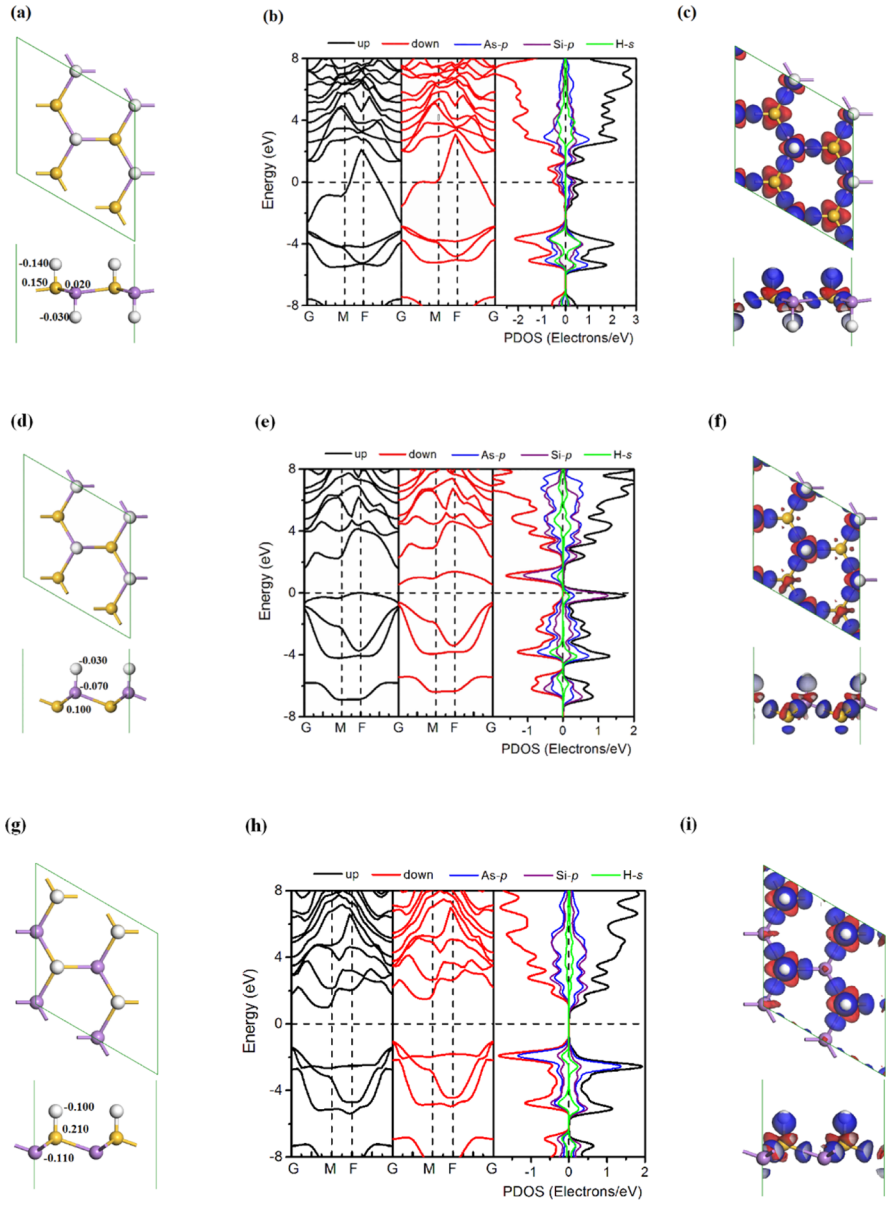

Figure 3. Optimized geometric structure (a,d,g), band structure, DOS (b,e,h), and charge density difference (c,f,i) of HAsSiH NS, HAsSi NS and AsSiH NS, respectively. The white balls denote H atoms. The parameters of lines and isosurfaces are the same as before.

In order to confirm the dynamical stability of the monolayer AsSi NS, the phonon dispersion is calculated and displayed in Figure 1b. The acoustic vibration frequencies and optic vibration frequencies of the monolayer AsSi NS are in the regions of 0−5.10 and 7.46−8.07 THz, respectively. The phonon mode is completely positive along the high symmetric points in the Brillouin zone, suggesting that the single-layered pristine AsSi NS is dynamically stable.

With the optimized structures of monolayer AsSi NS and confirmed structural stability, we now turn our attention to the electronic properties. The spin-polarized and the non-spin-polarized states are both considered for the AsSi NS system. The calculated results show that the total energy of the former is 434 meV per supercell lower than that of the latter, which indicates that the AsSi NS prefers the ferromagnetic ground state. In order to avoid finite-size effects, we performed some test calculation using a 3 × 3 supercell containing 18 atoms and a 4 × 4 supercell containing 32 atoms to check the convergence of our calculated results, which indicate that the magnetic moment and total energy difference between the spin-polarized and non-spin-polarized states are in good agreement with the calculated results based on the 2 × 2 supercell. These confirm that a 2 × 2 supercell of AsSi NS is sufficient for studying ferromagnetism. For the *k*-point sampling, test calculations using up to 27 × 27 × 1 Monkhorst−Pack *k*-points verified that the former *k*-mesh provides good convergence with respect to total energy differences and magnetic moment formation. The spin-polarized band structure in the hexagonal BZ for the AsSi NS is depicted in Figure 2a, and the Fermi level is set to zero. In order to deeply understand the contribution of different orbitals to the electronic states, total density of states (DOS) and partial DOS (PDOS) are also carried out and the results are summarized in Figure 2a. Compared with the band character of arsenene and silicene, the newly constructed AsSi NS exhibits a magnetic half-metallic character, where the spin-

DOI: 10.1021/acs.jpcc.9b01630
J. Phys. Chem. C 2019, 123, 14999−15008

up and spin-down states show the semiconducting and metallic behaviors, respectively. The spin-up state of the AsSi NS is an indirect band gap of 1.579 eV, where both the conduction band minimum (CBM) and valence band maximum (VBM) are located between Gamma (Γ) and *M* points. In the spin-down state, only one spin channel located slightly across the Fermi level.

The electronic distributions' charge transfer in the AsSi NS is analyzed by the Mulliken charge analysis.[55] The results indicate that the same atoms are equivalent and $e_{As} = -0.19$ and $e_{Si} = 0.19$ in charge transfer. In order to gain more insights into the bonding of As−Si, we have calculated the electron density difference to visualize the electron distribution of AsSi NS shown in Figure 2b. Clearly, electrons are depleted on the Si and As atoms (red area), whereas they are piled up on the bond of As and Si atoms (blue area), which exhibits the covalent nature and are corresponding to the Mulliken charge analysis. The origin of the magnetic behavior is further investigated by plotting the spin density distribution ($\Delta\rho = \rho_{up} - \rho_{down}$), as shown in Figure 2c. The total magnetic moment is 2 μB per 2 × 2 supercell. The magnetic moment mainly comes from As atom of 1.16 μB, whereas the Si atom carries a comparatively small net magnetic moment of about 0.84 μB.

To further assess the stability of monolayer AsSi NS, the formation energy E_{form} is defined as[59]

$$E_{form} = (E_{total} - n_1 \times E_1 - n_2 \times E_2)/(n_1 + n_2) \quad (2)$$

where E_{total} is the total energy of monolayer AsSi NS, E_1 and E_2 are the energies of a Si and As atoms in their solid phases, respectively, and n_1 and n_2 are the number of each element in the supercell, respectively. According to eq 2, E_{form} of AsSi NS is −0.358 eV/atom, which is smaller than the monolayer AsSi of −0.145 eV/atom.[59]

Following the idea of hydrogenated graphene, ZnO[60] and h-BN[61] NSs, we first study the fully hydrogenated AsSi NS. In order to search the most stable structures of hydrogenated AsSi NS systems, the energy with different lattice parameters is calculated. According to the minimum energy principle, the system with the lowest ground state energy is the most stable. Therefore, when the lattice parameter (a) increases to 4.32 Å, the fully hydrogenated AsSi NS (labeled as HAsSiH NS) has the lowest energy and exhibits the most stable structure. The relaxed atomic configuration of HAsSiH NS from the top and side views is shown in Figure 3a. The geometric optimization shows that the AsSi surface becomes even planar and all H atoms are adsorbed onto As and Si with H−As and Si−H bonds arranged perpendicularly to the AsSi plane. As also shown in Table 1, the optimized As−Si bond length is 2.498 Å; the hydrogen atoms are adsorbed on the top site of As and Si atoms with H−As and Si−H bond lengths of 1.529 and 1.500 Å, respectively, which are comparable to the bond lengths of 1.511 and 1.502 Å for the corresponding fully hydrogenated arsenenes[47] and silicone[59] and indicate the formation of strong chemical bonds between hydrogen, As, and Si atoms. The distance between As and Si planes, which is the buckling height (Δ) of fully hydrogenated HAsSiH, is found to be 0.169 Å, which is smoother and almost decreased to zero. The corresponding bond angle ∠AsSiAs increases to 118.532° on average. The atomic charge transfers in the HAsSiH nanosheet are analyzed by the Mulliken charge analysis, where H atoms adsorbed on As and Si atoms are carrying charges of −0.03 and −0.14 electrons, respectively. The buckling parameter decreases from 0.556 to 0.169 Å, which means a notable structure transformation from buckling to planar. To study the energetics of hydrogenation, we have calculated binding energy of HAsSiH, which is defined as the energy difference between the hydrogenated AsSi sheet, pristine AsSi sheet, and H atom. The hydrogenation of AsSi sheet is endothermic with an energy of −3.248 eV per supercell according to eq 1, which means that the system is rather stable in defending the thermal fluctuation in room temperature and can be experimentally fabricated. Meanwhile, the stability of the HAsSiH NS has been approved by the phonon dispersion calculation and is shown in Figure 1c. All branches of the phonon spectrum are positive, and no imaginary phonon mode exists, indicating that the HAsSiH NS exhibits well thermodynamic stability. The spin-polarized band structures and DOS of HAsSiH NS are shown in Figure 3b. The two bands cross the Fermi level, and there is no band gap opening for both spin-up and spin-down states, which displays a distinguished metallic behavior and is totally different from fully hydrogenated graphene. Hydrogenation opens a band gap in graphene, whereas it reduces the band gap in the AsSi NS and exhibits a transformation from semimetallic to metallic. This conspicuous difference indicates that the structural and electronic properties of AsSi NSs are also very sensitive to hydrogen decoration. Our calculation result shows that the total magnetic moment μ_{total} of the HAsSiH NS equals to 2 μB per 2 × 2 supercell, which shows that the HAsSiH NS is still a significant magnetic material. To reveal the origin of magnetism of HAsSiH, its PDOS and spin density distribution are investigated. It is also obvious to see the magnetism of HAsSiH through the spin PDOS in Figure 3b, where the PDOS strengths of p orbitals are unsymmetrical. Especially in the energy region near the Fermi level, the p orbital of As and Si atoms mainly contributes to the magnetic moment and the spin-down states are at a relatively higher energy level than those of spin-up states, which is consistent with the results obtained from PDOS. In addition, as shown in the spin density distribution of Figure S1a (Supporting Information), the spin-polarized magnetization still mainly comes from As atoms of 0.84 μB and Si atoms of 1.12 μB, whereas the H atoms bonded with Si atom only present 0.04 μB per supercell. Similarly, we have calculated the electron density difference to visualize the electron redistribution of HAsSiH, as shown in Figure 3c. The electron density difference can be used to quantify the bond overlap as well as the charge transfer from Si to H atoms, where the electrons are depleted on the Si atoms (red area).

As stated in previous discussions, the fully hydrogenation of the AsSi NS is an endothermic process. Once fully hydrogenated, H can strongly bind on As and Si sites. Starting from the fully hydrogenated AsSi NS, when removing the surface modification atoms of 2D material from one side, the structure transforms from fully HAsSiH NS to semihydrogenated AsSi NS and how will the structural and electronic properties change?

In a graphene sheet, all of the C sites are equivalent. Thus, when removing half of H atoms from a fully hydrogenated graphene sheet (graphane), there is only one option for the semihydrogenated graphene sheet.[62] However, in the AsSi NS, As and Si sites in the AsSi NS are chemically nonequivalent and then semihydrogenation can be accomplished by removing H from either Si sites (labeled as HAsSi) or all of the As sites (labeled as AsSiH), which is similar to Zn and O sites in ZnO NSs.

DOI: 10.1021/acs.jpcc.9b01630
J. Phys. Chem. C 2019, 123, 14999−15008

The structural parameters, electronic, and magnetic results of the two semi-hydrogenation structures are summarized in Tables 1 and 2. Correspondingly, we have plotted the spin-polarized band structure, PDOS, and charge density difference of HAsSi and AsSiH systems, as shown in Figure 3 e,f,h,i, respectively.

Table 2. Atom Mulliken Charges and Magnetic Moments (in μ_B) of Different Structures[a]

structure	AsSi NS	HAsSiH	HAsSi	AsSiH
e_{Si}	0.19	0.15	0.07	0.21
e_{As}	−0.19	0.02	−0.03	−0.11
e_H		−0.14 (H_1)	−0.04	−0.10
		−0.03 (H_2)		
μ_{Si}	1.16	1.12	1.24	0.72
μ_{As}	0.84	0.84	0.60	1.16
μ_H		0.04 (H_1)	0.16	0.12
		0.00 (H_2)		
μ_{total}	2	2	2	2

[a]The unit of the atom charge is one electron charge |e|. H_1 and H_2 mean that the H atom bonds with Si and As atom, respectively.

According to eq 2, E_{form} of HAsSi, AsSiH, and HAsSiH NSs is −0.183, −0.058, and −0.333 eV/atom, respectively, which means that our fully and partially hydrogenated AsSi NSs are stable. Meanwhile, we have calculated the phonon dispersion curves of HAsSi and AsSiH NSs with primitive structures to assess the structural stability and discuss the possibility in the experimental preparation, which are shown in Figure 1d,e, where all branches of the phonon dispersion curves have positive frequencies and no imaginary phonon modes are found, confirming the stability of semihydrogenated AsSi NS systems. To better examine the thermal stability of these systems, the total potential energy fluctuations with respect to time of fully and partially hydrogenated AsSi NSs at 300 K are calculated and shown in Figure S2 (Supporting Information). A 3 × 3 × 1 supercell is built to simulate the 2D sheet for minimizing the constraint caused by periodicity. The insets in Figure S2 show the atomic configuration of fully and partially hydrogenated AsSi NSs at the end of MD simulation. It is found that for fully and partially hydrogenated AsSi NSs, the total potential energy curves tend to stable values during the last 1 ps of simulation times and the atomic structures are almost invariant after heating for 2 ps at 300 K. Therefore, it is concluded that fully and partially hydrogenated AsSi NSs are thermally stable at 300 K.

The binding energy E_b is used to assess the structural stability of semihydrogenated AsSi NS systems. E_b of HAsSi and AsSiH NSs is −2.090 and −3.317 eV per supercell, respectively. Both of them have the negative values, which mean their outstanding dynamic stability. In addition, E_b of the H atoms absorb onto Si is more energetically favorable, which is comparatively lower than that onto As atoms. Thus, a more stable configuration of semihydrogenated AsSi NS is the one wherein all H atoms are adsorbed onto Si atoms, as shown in Figure 3d and more attention is paid on the AsSiH NS in the following discussion.

Compared with the buckling heights of pristine AsSi NS and fully hydrogenated HAsSiH NS, we can easily find that the buckling heights and corresponding bond angles ∠AsSiAs of semihydrogenated AsSi NS systems are both smaller than that of the HAsSiH NS and larger than that of the pristine AsSi NS. At the same time, both of the semihydrogenated AsSi NS systems have magnetic properties and ferromagnetic coupling, indicating that controlling the coverage of hydrogen cannot change the magnetic properties of AsSi NSs. The total magnetic moments of HAsSi and AsSiH systems are also shown in Table 2.

More careful examination of the spin-polarized band structure of the semi-hydrogenated AsSi NS system reveals appealing properties. By analyzing the magnetic source of HAsSi and AsSiH systems, the spin polarization is evident in the band structure and PDOS in Figure 3e,h. By the GGA−PBE method, HAsSi and AsSiH systems are both magnetic semiconductors with the band gaps of 0.544 and 2.040 eV, respectively. In addition, the band structures of decorated HAsSi and AsSiH systems have been corrected as 0.596 and 2.327 eV by the HSE06 hybrid functional in Figure 4, respectively, and the values of the band gap are also shown in the parentheses of Table 1.

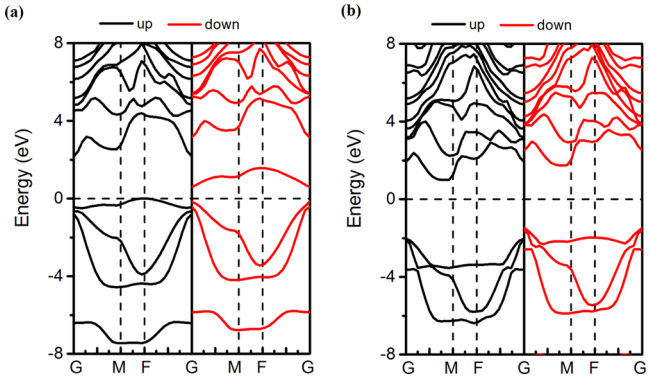

Figure 4. Band structures of decorated HAsSi (a) and AsSiH (b) systems by HSE06 hybrid functional. Black and red solid lines denote spin up and spin down band, respectively. The Fermi level is set to zero and indicated by black dashed line.

As described in Figure 3e, the semihydrogenated HAsSi system behaves as a magnetic semiconductor with band gaps of 1.583 and 1.192 eV in the spin-up and spin-down states. It is also obvious to see the magnetism of HAsSi system through the spin PDOS, where the PDOS strengths of Si p orbitals are unsymmetrical, especially in the energy region near the Fermi level. It is found from Figure 3e that the spin-up state is at a relatively higher energy level than those of the spin-down state. The contribution to DOS mainly comes from the p orbital of the spin-down state, which contributes the CBM. The VBM locates at *F* point of the spin-up state, whereas the CBM is at Γ point of spin-down state. Although for the AsSiH system in Figure 3h, it behaves as an indirect magnetic semiconductor with band gaps of 2.394 and 3.236 eV in the spin-up and spin-down states, respectively. The magnetism of the AsSiH system is originated from the unsymetricity of p orbitals of unpaired As atoms. However, the VBM locates at Γ point of the spin-down state, whereas the CBM is between Γ and *M* points of the spin-up state. Thus, controlling the coverage of hydrogen and the geometry is the key to observing the predicted electronic properties.

In fact, semihydrogenation on As atoms (Si atoms) forms strong As−H (Si−H) bonds and leaves the dangling bonds of surface As (Si) atoms spin unpaired in the HAsSi (AsSiH) system. The origin of the magnetic behavior is further

DOI: 10.1021/acs.jpcc.9b01630
J. Phys. Chem. C 2019, 123, 14999−15008

investigated by plotting the spin density distribution, as shown in Figure S1b,c. In the two cases, the spin-polarized magnetization distinctly distributed (the blue region) on the undecorated Si (1.24 μ_B) or As (1.16 μ_B) atoms, when the spin value is set to be 0.03 e/Å^3. Obviously, the emergent spin polarization is not restricted to the surface As atoms (Si atoms) but instead is delocalized uniformly in the entire system, leading to a net magnetic moment of approximately 2 μ_B per supercell. The contributions from H and corresponding saturated Si atom (As atom) are 0.12 μ_B (0.16 μ_B) and 0.72 μ_B (0.60 μ_B) for the AsSiH (HAsSi) system, which is consistent with the results obtained from PDOS, as shown in Figure 3.

In order to achieve deeper insights into the bonding of H−Si, we have further calculated the electron density difference to visualize the electron redistribution of semihydrogenated AsSiH NSs in Figure 3i. Clearly, electrons are depleted on the Si atoms (red area), whereas they are piled up on H and As atoms (blue area). Moreover, electron orbital overlap of the AsSiH NS is observed. In addition, the Mulliken charges and charge transfers have also analyzed. The variation of the number of electrons on As, Si, and H atoms is shown in Figure 3g. Clearly, the Si atom is positively charged with the charge of 0.210e, whereas electrons will accumulate on As and H atoms, making them negatively charged with the charges of −0.110e and −0.100e, respectively. Because the electronegativity of Si atom is weaker than that of H atoms, each Si transfers −0.100e to H atoms and they interact covalently with each other via σ bonding. Such charge distribution is consistent with its distribution of magnetic moment, which is an important factor to induce the magnetism in the AsSiH NS.

We also simulated the optical absorption spectra of these systems to further examine whether they meet the criteria for efficient visible-light absorption. The optical properties such as the real part ε_1 and imaginary part ε_2 of complex dielectric function and absorption coefficient $\alpha(\omega)$ can be determined by following formulas[11]

$$\varepsilon_1(\omega) = \frac{1}{\pi} P \int_{-\infty}^{\infty} \frac{\varepsilon_2(\omega')}{\omega' - \omega} \, d\omega' \tag{3}$$

$$\varepsilon_2(\omega) = \frac{2e^2\pi}{\Omega\varepsilon_0} \sum_{k,\,c,\,v} |\langle \Psi_k^{\,c} | \mathbf{u}\cdot\mathbf{r} | \Psi_k^{\,v} \rangle|^2 \delta(E_k^{\,c} - E_k^{\,v} - E) \tag{4}$$

$$\alpha(\omega) = \sqrt{2}\,\omega[\sqrt{\varepsilon_1^{\,2}(\omega) + \varepsilon_2^{\,2}(\omega)} - \varepsilon_1(\omega)]^{1/2} \tag{5}$$

where ω denotes the frequency of the electromagnetic radiation in energy unit. Ω represents the cell volume, and ε_0 is the dielectric constant in free space. c and v represent the conduction and valence band states, respectively. P is the principal value of the integral. In addition, $\mathbf{u}$ and $\mathbf{r}$ denote the vector defining the polarization of the incident electric field and the position vector, respectively. Here, $\alpha(\omega) = \sqrt{\varepsilon_1^{\,2}(\omega) + \varepsilon_2^{\,2}(\omega)}$ is the relative dielectric constant. The electric field vectors are both perpendicular ($E_\perp$) and parallel ($E_\parallel$) to the structure. Because of the symmetry of the lattice structure, the optical absorption intensity is significantly weaker under $E_\perp$ than that under $E_\parallel$ in the visible region. Therefore, in the following, we mainly discuss the optical results from the latter. Figure 5a clearly shows that the absorption intensity of the AsSiH NS is very strong with values more than 10^4 cm^{-1}, which is able to harvest visible light.[63]

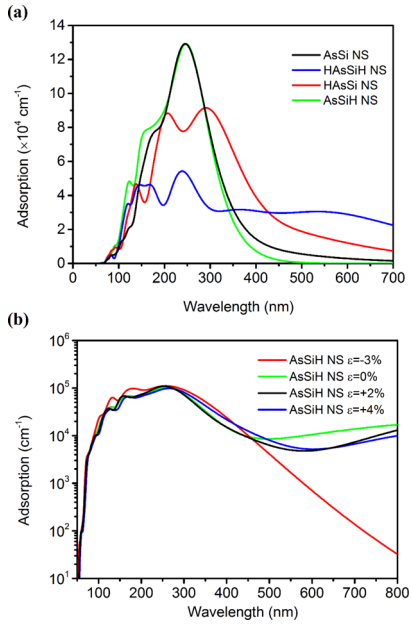

Figure 5. Optical absorption coefficients of the four systems (a) and the optical absorption spectra of AsSiH NS without and with strains (b).

Applying external strain ε has been known as the effective method to control electronic, transport, and optical properties of materials for semiconductors for decades.[64,65] In order to ensure the stability of AsSiH NS in the range of external strain, we have carefully observed the changes of the structure and energy difference ΔE. As shown in Figure S3, $\Delta E = E_\varepsilon - E_0$, where E_0 is the lowest energy of the corresponding AsSiH NS without the biaxial strains. It is found that even applying the strain from −10 to +10%, the deformation of structure is comparatively small and the structural integrity is well maintained withstand the biaxial strain.

Meanwhile, the optical absorption spectra of the AsSiH NS without and with strains calculated are plotted in Figure 5b. The changing trend of the light absorption intensity that we obtained before and after applying stress is obtained. The compressive strain can reduce the light absorption, whereas the suitable tensile strains in AsSiH NS are efficient ways for extending the light absorption region. Figure 6 displays the calculated VBM and CBM positions for AsSiH NSs under

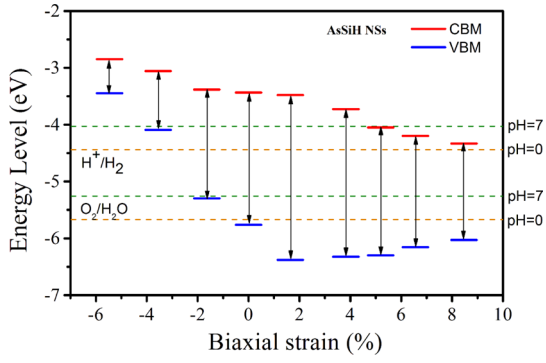

Figure 6. Band edge positions of strained AsSiH nanosheet relative to the vacuum potential level. The orange and olive dashed lines represent the standard reduction potential of H^+/H_2 and the oxidation potential of O_2/H_2O at pH = 0 and pH = 7, respectively.

DOI: 10.1021/acs.jpcc.9b01630
J. Phys. Chem. C 2019, 123, 14999−15008

various biaxial strains from −6 to 9% relative to the vacuum level. To effectively photocatalyze the splitting of water, suitable alignment of the band edge to straddle the redox potentials of water splitting reaction is an essential requirement and the band gap should be larger than 1.23 eV and smaller than 3 eV in order to enhance the solar light absorption.[66−69]

As shown in Figure 6, for the initial AsSiH structure, the value of CBM is at −3.44 eV, which is about 1.0 eV higher than the water reduction potential of H^+/H_2 (−4.44 eV with respect to the vacuum level) and the value of VBM is at −5.76 eV, which is about 0.09 eV lower than the oxidation potential of O_2/H_2O (−5.67 eV with respect to the vacuum level). As compressive strain is applied and above −2%, the VBM level shifts upward and the reduction reaction becomes energetically impossible. However, with increasing the tensile strain, the VBM level shifts downward, even for the AsSiH NS under the tensile strain up to 9%, the CBM energy level is still located about 0.07 eV higher than the water reduction potential of H^+/H_2 and the VBM energy level is still located about 0.31 eV lower than the oxidation potential of O_2/H_2O. Despite the ubiquity and easy introduction of tensile strains in monolayers, it is found that the spatial distributions of the VBM and CBM of AsSiH NS are not notably affected by the uniaxial tensile strains. Such a desirable band edge alignment renders AsSiH NS a possible effective visible-light-driven photocatalyst for the water-splitting reaction.

It should be noted that the water redox potential depends on the pH value.[70] The standard oxidation potential of O_2/H_2O in a solution can be calculated by $E^{OX}_{O_2/H_2O} = -5.67\ eV + pH \times 0.059\ eV$, and the reduction potential for H^+/H_2 is determined by $E_{H^+/H_2}{}^{red} = -4.44\ eV + pH \times 0.059\ eV$. Thus, the redox potential in a neutral environment (pH = 7) is also studied. From Figure 6, surprisingly, the band edges of the AsSiH NS under the tensile strain below 4% can still straddle the water redox potential even at pH = 7. These results provide eloquent evidence that the AsSiH NS might have promising applications for hydrogen generation in both neutral and acidic environments by water splitting.

4. CONCLUSIONS

In summary, we have systematically investigated the modulation of structural, electronic, and magnetic properties of hydrogenated AsSi NSs using first-principles calculations, which provides an attractive landscape for both fundamental research and practical applications with 2D magnetic materials. We have demonstrated that fully and semihydrogenated AsSi NSs exhibit ferromagnetism states and AsSi NSs undergo transitions from half-metallic to metallic and then into semiconductive states. Therefore, surface passivation by H atoms serves as an important approach in tailoring the electronic properties of AsSi NSs. In addition, AsSiH NSs with tensile strains up to 9% exhibit proper band gaps, valence, and conduction band positions of the reduction and oxidation levels in visible-light-driven water splitting. These diverse properties are of fundamental significance and may be a promising candidate for future 2D magnetic material used in spintronic and optoelectronic devices.

■ ASSOCIATED CONTENT

Supporting Information

The Supporting Information is available free of charge on the ACS Publications website at DOI: 10.1021/acs.jpcc.9b01630.

Isosurfaces of spin density distribution (PDF)

■ AUTHOR INFORMATION

Corresponding Author

*E-mail: hecheng@mail.xjtu.edu.cn.

ORCID

W.X. Zhang: 0000-0002-9327-5761

C. He: 0000-0002-6612-5346

Notes

The authors declare no competing financial interest.

■ ACKNOWLEDGMENTS

The authors acknowledge supports by National Key Basic Research and Development Program (grant no. 2015CB655105), National Natural Science Foundation of China (NSFC, nos. 51471124, 51608041, and 11604022), Natural Science Foundation of Shaanxi province, China (2019JM-189), the Fundamental Research Funds for the Central Universities (no. xjj2016018), and National Training Programs of Innovation and Entrepreneurship for Undergraduates (201810710128).

■ REFERENCES

(1) Chen, J.; Zhu, E.; Liu, J.; Zhang, S.; Lin, Z.; Duan, X.; Heinz, H.; Huang, Y.; De Yoreo, J. J. Building Two-Dimensional Materials One Row at a Time: Avoiding the Nucleation Barrier. *Science* **2018**, *362*, 1135.

(2) Fei, Z.; Zhao, W.; Palomaki, T. A.; Sun, B.; Miller, M. K.; Zhao, Z.; Yan, J.; Xu, X.; Cobden, D. H. Ferroelectric Switching of a Two-Dimensional Metal. *Nature* **2018**, *560*, 336.

(3) Keerthi, A.; Geim, A. K.; Janardanan, A.; Rooney, A. P.; Esfandiar, A.; Hu, S.; Dar, S. A.; Grigorieva, I. V.; Haigh, S. J.; Wang, F. C.; Radha, B. Ballistic Molecular Transport through Two-Dimensional Channels. *Nature* **2018**, *558*, 420.

(4) Tang, H.-K.; Leaw, J. N.; Rodrigues, J. N. B.; Herbut, I. F.; Sengupta, P.; Assaad, F. F.; Adam, S. The Role of Electron-Electron Interactions in Two-Dimensional Dirac Fermions. *Science* **2018**, *361*, 570−574.

(5) Li, Q.; Zhao, Z.; Yan, B.; Song, X.; Zhang, Z.; Li, J.; Wu, X.; Bian, Z.; Zou, X.; Zhang, Y.; Liu, Z. Nickelocene-Precursor-Facilitated Fast Growth of Graphene/h-BN Vertical Heterostructures and Its Applications in Oleds. *Adv. Mater.* **2017**, *29*, 1701325.

(6) Kvashnin, D. G.; Matveev, A. T.; Lebedev, O. I.; Yakobson, B. I.; Golberg, D.; Sorokin, P. B.; Shtansky, D. V. Ultrasharp h-BN Nanocones and the Origin of Their High Mechanical Stiffness and Large Dipole Moment. *J. Phys. Chem. Lett.* **2018**, *9*, 5086−5091.

(7) Xiao, M.; Yao, T.; Ao, Z.; Wei, P.; Wang, D.; Song, H. Tuning Electronic and Magnetic Properties of Gan Nanosheets by Surface Modifications and Nanosheet Thickness. *Phys. Chem. Chem. Phys.* **2015**, *17*, 8692−8698.

(8) Banerjee, S.; Onnink, A. J.; Dutta, S.; Aarnink, A. A. I.; Gravesteijn, D. J.; Kovalgin, A. Y. Composite GaN-C-Ga ("GaCN") Layers with Tunable Refractive Index. *J. Phys. Chem. C* **2018**, *122*, 29567−29576.

(9) Li, Y.; Chen, Z. Tuning Electronic Properties of Germanane Layers by External Electric Field and Biaxial Tensile Strain: A Computational Study. *J. Phys. Chem. C* **2014**, *118*, 1148−1154.

(10) Dong, M. M.; He, C.; Zhang, W. X. Tunable Electronic Properties of Arsenene and Transition-Metal Dichalcogenide Heterostructures: A First-Principles Calculation. *J. Phys. Chem. C* **2017**, *121*, 22040−22048.

DOI: 10.1021/acs.jpcc.9b01630
J. Phys. Chem. C 2019, 123, 14999−15008

(11) Li, T. T.; He, C.; Zhang, W. X. Structural Complexity and Wide Application of Two-Dimensional S/O Type Antimonene. *Appl. Surf. Sci.* **2018**, *441*, 77−84.
(12) Eslamibidgoli, M. J.; Eikerling, M. H. Mechanical and Chemical Stability of Monolayer Black Phosphorous Studied by Density Functional Theory Simulations. *J. Phys. Chem. C* **2018**, *122*, 22366−22373.
(13) Dong, M. M.; He, C.; Zhang, W. X. A Tunable and Sizable Bandgap of a G-C_3N_4/Graphene/G- G-C_3N_4 Sandwich Heterostructure: A Van Der Waals Density Functional Study. *J. Mater. Chem. C* **2017**, *5*, 3830−3837.
(14) Li, L.; Yu, Y.; Ye, G. J.; Ge, Q.; Ou, X.; Wu, H.; Feng, D.; Chen, X. H.; Zhang, Y. Black Phosphorus Field-Effect Transistors. *Nat. Nanotechnol.* **2014**, *9*, 372−377.
(15) Zhou, L.; Zhang, J.; Zhuo, Z.; Kou, L.; Ma, W.; Shao, B.; Du, A.; Meng, S.; Frauenheim, T. Novel Excitonic Solar Cells in Phosphorene-TiO_2 Heterostructures with Extraordinary Charge Separation Efficiency. *J. Phys. Chem. Lett.* **2016**, *7*, 1880−1887.
(16) Peng, W.; Xu, T.; Diener, P.; Biadala, L.; Berthe, M.; Pi, X.; Borensztein, Y.; Curcella, A.; Bernard, R.; Prévot, G.; Grandidier, B. Resolving the Controversial Existence of Silicene and Germanene Nanosheets Grown on Graphite. *ACS Nano* **2018**, *12*, 4754−4760.
(17) Zhou, D.; Niu, Z.; Niu, T. Surface Reconstruction of Germanium: Hydrogen Intercalation and Graphene Protection. *J. Phys. Chem. C* **2018**, *122*, 21874−21882.
(18) Heo, J. H.; Kim, J.; Kim, H.; Moon, S. H.; Im, S. H.; Hong, K.-H. Roles of SnX_2 (X = F, Cl, Br) Additives in Tin-Based Halide Perovskites toward Highly Efficient and Stable Lead-Free Perovskite Solar Cells. *J. Phys. Chem. Lett.* **2018**, *9*, 6024−6031.
(19) Guo, S.; Hu, X.; Zhou, W.; Liu, X.; Gao, Y.; Zhang, S.; Zhang, K.; Zhu, Z.; Zeng, H. Mechanistic Understanding of Two-Dimensional Phosphorus, Arsenic, and Antimony High-Capacity Anodes for Fast-Charging Lithium/Sodium Ion Batteries. *J. Phys. Chem. C* **2018**, *122*, 29559−29566.
(20) Veber, A.; Cicconi, M. R.; Puri, A.; de Ligny, D. Optical Properties and Bismuth Redox in Bi-Doped High-Silica Al-Si Glasses. *J. Phys. Chem. C* **2018**, *122*, 19777−19792.
(21) Qin, R.; Chen, Z.-Y. Strain-Controlled High Harmonic Generation with Dirac Fermions in Silicene. *Nanoscale* **2018**, *10*, 22593−22600.
(22) Li, G.; Zhang, L. Z.; Xu, W. Y.; Pan, J. B.; Song, S. R.; Zhang, Y.; Zhou, H. T.; Wang, Y. L.; Bao, L. H.; Zhang, Y. Y.; Du, S. X.; Ouyang, M.; Pantelides, S. T.; Gao, H. J. Stable Silicene in Graphene/Silicene Van Der Waals Heterostructures. *Adv. Mater.* **2018**, *30*, 1804650.
(23) Le, P. T. T.; Hieu, N. N.; Bui, L. M.; Phuc, H. V.; Hoi, B. D.; Amin, B.; Nguyen, C. V. Structural and Electronic Properties of a Van Der Waals Heterostructure Based on Silicene and Gallium Selenide: Effect of Strain and Electric Field. *Phys. Chem. Chem. Phys.* **2018**, *20*, 27856−27864.
(24) Frombach, D.; Park, S.; Schroer, A.; Recher, P. Electrically Controlled Crossover between 2 π and 4π Josephson Effects through Topologically Confined Channels in Silicene. *Phys. Rev. B* **2018**, *98*, 205305.
(25) Ding, Y.; Wang, Y. Tunable Electronic Structures of Hydrogenated Zigzag and Armchair Dumbbell Silicene Nanosheets: A Computational Study. *J. Phys. Chem. C* **2018**, *122*, 23208−23216.
(26) Gao, Y.; Zhou, Y.; Zhang, X.; Hu, M. Extremely Low Thermal Conductivity of Polycrystalline Silicene. *J. Phys. Chem. C* **2018**, *122*, 9220−9228.
(27) Zhao, J.; Liu, H.; Yu, Z.; Quhe, R.; Zhou, S.; Wang, Y.; Liu, C. C.; Zhong, H.; Han, N.; Lu, J.; Yao, Y.; Wu, K. Rise of Silicene: A Competitive 2d Material. *Prog. Mater. Sci.* **2016**, *83*, 24−151.
(28) Cahangirov, S.; Topsakal, M.; Akturk, E.; Sahin, H.; Ciraci, S. Two- and One-Dimensional Honeycomb Structures of Silicon and Germanium. *Phys. Rev. Lett.* **2009**, *102*, 236804.
(29) Tsai, H.-S.; Chen, C.-W.; Hsiao, C.-H.; Ouyang, H.; Liang, J.-H. The Advent of Multilayer Antimonene Nanoribbons with Room Temperature Orange Light Emission. *Chem. Commun.* **2016**, *52*, 8409−8412.
(30) Ares, P.; Aguilar-Galindo, F.; Rodríguez-San-Miguel, D.; Aldave, D. A.; Díaz-Tendero, S.; Alcamí, M.; Martín, F.; Gómez-Herrero, J.; Zamora, F. Mechanical Isolation of Highly Stable Antimonene under Ambient Conditions. *Adv. Mater.* **2016**, *28*, 6332.
(31) Gibaja, C.; et al. Few-Layer Antimonene by Liquid-Phase Exfoliation. *Angew. Chem., Int. Ed.* **2016**, *55*, 14345.
(32) Ji, J.; Song, X.; Liu, J.; Yan, Z.; Huo, C.; Zhang, S.; Su, M.; Liao, L.; Wang, W.; Ni, Z.; Hao, Y.; Zeng, H. Two-Dimensional Antimonene Single Crystals Grown by Van Der Waals Epitaxy. *Nat. Commun.* **2016**, *7*, 13352.
(33) Chen, H.; Ye, F.; Tang, W.; He, J.; Yin, M.; Wang, Y.; Xie, F.; Bi, E.; Yang, X.; Grätzel, M.; Han, L. A Solvent- and Vacuum-Free Route to Large-Area Perovskite Films for Efficient Solar Modules. *Nature* **2017**, *550*, 92.
(34) Nozik, A. J.; Miller, J. Introduction to Solar Photon Conversion. *Chem. Rev.* **2010**, *110*, 6443−6445.
(35) Walter, M. G.; Warren, E. L.; McKone, J. R.; Boettcher, S. W.; Mi, Q.; Santori, E. A.; Lewis, N. S. Solar Water Splitting Cells. *Chem. Rev.* **2010**, *110*, 6446−6473.
(36) Chen, X.; Shen, S.; Guo, L.; Mao, S. S. Semiconductor-Based Photocatalytic Hydrogen Generation. *Chem. Rev.* **2010**, *110*, 6503−6570.
(37) Zhang, S.; Yan, Z.; Li, Y.; Chen, Z.; Zeng, H. Atomically Thin Arsenene and Antimonene: Semimetal-Semiconductor and Indirect-Direct Band-Gap Transitions. *Angew. Chem., Int. Ed.* **2015**, *54*, 3112−3115.
(38) Lopez-Bezanilla, A.; Ganesh, P.; Kent, P. R. C.; Sumpter, B. G. Spin-Resolved Self-Doping Tunes the Intrinsic Half-Metallicity of Aln Nanoribbons. *Nano Res.* **2014**, *7*, 63−70.
(39) Tang, Q.; Bao, J.; Li, Y.; Zhou, Z.; Chen, Z. Tuning Band Gaps of BN Nanosheets and Nanoribbons Via Interfacial Dihalogen Bonding and External Electric Field. *Nanoscale* **2014**, *6*, 8624−8634.
(40) Li, J.; Li, H.; Wang, Z.; Zou, G. Structure, Magnetic, and Electronic Properties of Hydrogenated Two-Dimensional Diamond Films. *Appl. Phys. Lett.* **2013**, *102*, 073114.
(41) Song, Z.; Liu, C.-C.; Yang, J.; Han, J.; Ye, M.; Fu, B.; Yang, Y.; Niu, Q.; Lu, J.; Yao, Y. Quantum Spin Hall Insulators and Quantum Valley Hall Insulators of Bix/Sbx (X = H, F, Cl and Br) Monolayers with a Record Bulk Band Gap. *NPG Asia Mater.* **2014**, *6*, No. e147.
(42) Zhou, J.; Wu, M. M.; Zhou, X.; Sun, Q. Tuning Electronic and Magnetic Properties of Graphene by Surface Modification. *Appl. Phys. Lett.* **2009**, *95*, 103108.
(43) Zhou, J.; Wang, Q.; Sun, Q.; Jena, P. Electronic and Magnetic Properties of a BN Sheet Decorated with Hydrogen and Fluorine. *Phys. Rev. B: Condens. Matter Mater. Phys.* **2010**, *81*, 085442.
(44) Shi, Z.; Zhao, X.; Huang, X. First Principles Investigation on the Stability, Magnetic and Electronic Properties of the Fully and Partially Hydrogenated BN Nanoribbons in Different Conformers. *J. Mater. Chem. C* **2013**, *1*, 6890−6898.
(45) Zhang, P.; Li, X. D.; Hu, C. H.; Wu, S. Q.; Zhu, Z. Z. First-Principles Studies of the Hydrogenation Effects in Silicene Sheets. *Phys. Lett. A* **2012**, *376*, 1230−1233.
(46) Gao, N.; Lu, G. Y.; Wen, Z.; Jiang, Q. Electronic Structure of Silicene: Effects of the Organic Molecular Adsorption and Substrate. *J. Mater. Chem. C* **2017**, *5*, 627−633.
(47) Zhang, S.; Hu, Y.; Hu, Z.; Cai, B.; Zeng, H. Hydrogenated Arsenenes as Planar Magnet and Dirac Material. *Appl. Phys. Lett.* **2015**, *107*, 022102.
(48) Seitz, A. E.; Eckhardt, M.; Erlebach, A.; Peresypkina, E. V.; Sierka, M.; Scheer, M. Pnictogen-Silicon Analogues of Benzene. *J. Am. Chem. Soc.* **2016**, *138*, 10433−10436.
(49) Segall, M. D.; Lindan, P. J. D.; Probert, M. J.; Pickard, C. J.; Hasnip, P. J.; Clark, S. J.; Payne, M. C. First-Principles Simulation: Ideas, Illustrations and the Castep Code. *J. Phys.: Condens. Matter* **2002**, *14*, 2717−2744.
(50) Perdew, J. P.; Burke, K.; Wang, Y. Generalized Gradient Approximation for the Exchange-Correlation Hole of a Many-

DOI: 10.1021/acs.jpcc.9b01630
J. Phys. Chem. C 2019, 123, 14999−15008

Electron System. *Phys. Rev. B: Condens. Matter Mater. Phys.* **1996**, *54*, 16533−16539.
(51) Vanderbilt, D. Soft Self-Consistent Pseudopotentials in a Generalized Eigenvalue Formalism. *Phys. Rev. B: Condens. Matter Mater. Phys.* **1990**, *41*, 7892−7895.
(52) Zhang, W. X.; He, W. H.; Zhao, J. W.; He, C. Electronic Properties of Blue Phosphorene/transition Metal Dichalcogenides van der Waals Heterostructures under in-plane Biaxial Strains. *J. Solid State Chem.* **2018**, *265*, 257−265.
(53) Dong, M. M.; He, C.; Zhang, W. X. A Tunable and Sizable Bandgap of a g-C_3N_4/graphene/g-C_3N_4 Sandwich Heterostructure: a van der Waals Density Functional Study. *J. Mater. Chem. C* **2017**, *5*, 3830−3837.
(54) Li, T.; He, C.; Zhang, W. A Novel Porous C_4N_4 Monolayer as a Potential Anchoring Material for Lithium−sulfur Battery Design. *J. Mater. Chem. A* **2019**, *7*, 4134−4144.
(55) Monkhorst, H. J.; Pack, J. D. Special Points for Brillouin-Zone Integrations. *Phys. Rev. B: Condens. Matter Mater. Phys.* **1976**, *13*, 5188−5192.
(56) He, C.; Zhang, P.; Zhu, Y. F.; Jiang, Q. Structures and Quantum Conduction of Copper Nanowires under Electric Fields Using First Principles. *J. Phys. Chem. C* **2008**, *112*, 9045−9049.
(57) Davidson, E. R.; Chakravorty, S. A Test of the Hirshfeld Definition of Atomic Charges and Moments. *Theor. Chim. Acta* **1992**, *83*, 319−330.
(58) Li, S.; Wu, Y.; Liu, W.; Zhao, Y. Control of Band Structure of Van Der Waals Heterostructures: Silicene on Ultrathin Silicon Nanosheets. *Chem. Phys. Lett.* **2014**, *609*, 161−166.
(59) Zhou, L.; Guo, Y.; Zhao, J. GeAs and SiAs Monolayers: Novel 2d Semiconductors with Suitable Band Structures. *Phys. E* **2018**, *95*, 149−153.
(60) Tang, W.; Sun, M.; Ren, Q.; Wang, S.; Yu, J. Halogenated Arsenenes as Dirac Materials. *Appl. Surf. Sci.* **2016**, *376*, 286−289.
(61) Lin, S.; Gu, J.; Wang, Y.; Wang, Y.; Zhang, S.; Liu, X.; Zeng, H.; Chen, Z. Porous Silaphosphorene, Silaarsenene and Silaantimonene: A Sweet Marriage of Si and P/As/Sb. *J. Mater. Chem. A* **2018**, *6*, 3738−3746.
(62) Tang, Q.; Li, Y.; Zhou, Z.; Chen, Y.; Chen, Z. Tuning Electronic and Magnetic Properties of Wurtzite ZnO Nanosheets by Surface Hydrogenation. *ACS Appl. Mater. Interfaces* **2010**, *2*, 2442−2447.
(63) Ma, X.; Wu, X.; Wang, H.; Wang, Y. A Janus Mosse Monolayer: A Potential Wide Solar-Spectrum Water-Splitting Photocatalyst with a Low Carrier Recombination Rate. *J. Mater. Chem. A* **2018**, *6*, 2295−2301.
(64) Castellanos-Gomez, A.; Roldán, R.; Cappelluti, E.; Buscema, M.; Guinea, F.; van der Zant, H. S. J.; Steele, G. A. Local Strain Engineering in Atomically Thin MoS_2. *Nano Lett.* **2013**, *13*, 5361−5366.
(65) Ma, Y.; Dai, Y.; Guo, M.; Niu, C.; Zhu, Y.; Huang, B. Evidence of the Existence of Magnetism in Pristine VX_2 Monolayers (X = S, Se) and Their Strain-Induced Tunable Magnetic Properties. *ACS Nano* **2012**, *6*, 1695−1701.
(66) Zhou, J.; Wang, Q.; Sun, Q.; Chen, X. S.; Kawazoe, Y.; Jena, P. Ferromagnetism in Semihydrogenated Graphene Sheet. *Nano Lett.* **2009**, *9*, 3867−3870.
(67) Yang, H.; Li, J.; Yu, L.; Huang, B.; Ma, Y.; Dai, Y. A Theoretical Study on the Electronic Properties of In-Plane CdS/ZnSe Heterostructures: Type-II Band Alignment for Water Splitting. *J. Mater. Chem. A* **2018**, *6*, 4161−4166.
(68) Kudo, A.; Miseki, Y. Heterogeneous Photocatalyst Materials for Water Splitting. *Chem. Soc. Rev.* **2009**, *38*, 253−278.
(69) Liao, P.; Carter, E. A. New Concepts and Modeling Strategies to Design and Evaluate Photo-Electro-Catalysts Based on Transition Metal Oxides. *Chem. Soc. Rev.* **2013**, *42*, 2401−2422.
(70) Li, L.; Li, P. F.; Lu, N.; Dai, J.; Zeng, X. C. Simulation Evidence of Hexagonal-to-Tetragonal ZnSe Structure Transition: A Monolayer Material with a Wide-Range Tunable Direct Bandgap. *Adv. Sci.* **2015**, *2*, 8.

DOI: 10.1021/acs.jpcc.9b01630
J. Phys. Chem. C 2019, 123, 14999−15008